Journal of Alloys and Compounds 799 (2019) 256–266

Contents lists available at ScienceDirect

Journal of Alloys and Compounds

journal homepage: http://www.elsevier.com/locate/jalcom

Eco-friendly synthesis of porous graphene and its utilization as high performance supercapacitor electrode material

Meenaketan Sethi [a], Harsha Bantawal [a], U. Sandhya Shenoy [b], D. Krishna Bhat [a, *]

[a] Department of Chemistry, National Institute of Technology Karnataka, Surathkal, Mangalore, 575025, India
[b] Department of Chemistry, College of Engineering and Technology, Srinivas University, Mukka, Mangalore, 574146, India

ARTICLE INFO

Article history:
Received 21 December 2018
Received in revised form
4 May 2019
Accepted 27 May 2019
Available online 28 May 2019

Keywords:
Porous graphene
Solvothermal method
Surface area
Supercapacitor
Cyclic stability

ABSTRACT

The successful application of porous graphene (PG) is hindered due to the lack of efficient and cost-effective method for its synthesis. Herein, we report a facile and eco-friendly method to produce PG through a low temperature solvothermal method. The structural and morphological characteristics of PG samples were investigated thoroughly. The as synthesized material is found to be a few layers thick (~4 −6 layers) with a surface area of 420 $m^2 g^{-1}$ and consisting of hierarchical pores on the surface of the sheets. A high specific capacitance of 666 F g^{-1} was obtained at a scan rate of 5 mV s^{-1}, apart from longer cyclic stability with 87% retention of initial capacitance value after 10000 cycles for the PG 28 sample. The fabricated supercapacitor displayed an energy density of 26.3 Wh kg^{-1} and power density of 6120 W kg^{-1}. Density functional theory calculations were also carried out to qualitatively support the enhanced capacitance by providing theoretical insight from electronic structure and density of states of PG. These results open a new avenue for greener synthesis of high-quality PG using environmentally friendly solvents, without the use of toxic chemicals, for excellent supercapacitor performance.

1. Introduction

Porous Graphene (PG) is a type of spongy graphenic material, which possesses different properties compared to that of graphene. After the discovery of graphene, many researchers have tried to modify the parent graphene structure and created a new type of planar sheet structure consisting of pores viz PG, formed by the removal of sp^2 bonded carbon atoms. Depending on their pore diameters they are classified as microporous (diameter < 2 nm), mesoporous (diameter from 2 to 50 nm), and macroporous (diameter >50 nm) materials [1]. The pore sizes also vary from atomic to nanoscale dimensions, based on the fabrication methods used. Microporous structures can be used in catalysis, water and air purification whereas the mesoporous and macroporous structures are generally used in adsorption of large hydrophobic molecules, chromatographic separations, and electrochemical capacitors [2].

Although there are several reports on the synthesis of PG and its utilization for charge storage, they involve use of strong oxidants, templates or chemical activation. An overview of the recent literature reveals that in such methods the production cost is high, the yield is poor, capacitance is less, or capacitance retention is low apart from lower energy and power densities [3–8]. These factors limit its applicability in a real-world market. In most of the cases, the planar graphene sheets readily agglomerate owing to either van der Waals or capillary forces due to which it hinders the efficient transport of electrons across the channels and hence, the effective utilization of the planar sheet is not possible to improve the electrochemical performance of the material [9]. In this paper, for the first time, we report the synthesis of PG with high surface area by a low-cost and eco-friendly method for mass production, employing an energy matching solvent system consisting of a mixture of 1:1 ethylene glycol and water (EG + H_2O). Study of its supercapacitor performance in terms of specific capacitance and cyclability has also been carried out. The superior electrochemical activity observed has been mainly attributed to the high surface area of graphene sheets and its hierarchical porous structure which is highly beneficial for the efficient storage of charges and transport of ions, which in turn enhances the supercapacitor performance. We have also carried out first principles density functional theory (DFT) calculations to show the enhancement of charge bearing capacity of PG over graphene.

* Corresponding author.
E-mail address: denthajekb@gmail.com (D.K. Bhat).

https://doi.org/10.1016/j.jallcom.2019.05.302
0925-8388/

2. Experimental section

2.1. Materials

All the chemicals used were of analytical grade and were used without any further purification. Deionized water was used for washing and preparation of graphene oxide (GO) suspension and PG.

2.2. Methods

2.2.1. Synthesis of GO

GO was synthesized according to the improved Hummers' method, reported elsewhere [10]. A calculated amount of graphite was mixed with 9:1 mixture of H_2SO_4: H_3PO_4. $KMnO_4$ was added in batches of little amount with continuous stirring to avoid overheating and then the reaction mixture was maintained at 50 °C for 12 h. The dark brown suspension formed was poured into 200 mL ice water followed by the addition of 30% H_2O_2 till the effervescence ceases, changing the color of the suspension from dark brown to brilliant yellow. The suspension was successively washed with water, 30% HCl and ethanol and finally dried at 50 °C for 10 h to get GO.

2.2.2. Synthesis of PG

The obtained GO was dispersed in a mixture of 1:1 EG + H_2O (1 mg/mL) and was ultrasonicated for 2–3 h in an ultrasonic bath. Then, the exfoliated GO dispersion was put into a stainless-steel autoclave of 100 mL capacity and further heated to 160 °C for 16–32 h (these samples were named as PG 16 to PG 32, respectively). After the autoclave gets cooled down to room temperature, the black products were collected and were repeatedly washed with water. Finally, the products were dried at 80 °C for 6 h to obtain PG (Scheme 1).

2.2.3. Characterization

The structural and morphological characterizations of GO and PG were done by XRD (Rigaku MiniFlex 600 X-Ray diffractometer) with Cu K_α radiation ($\lambda = 1.5418$ Å), FESEM (Zeiss Ultra 55 field emission scanning electron microscope) and TEM (JEOL-TEM 2100 and FEI Tecnai G2). Raman spectra were recorded on a STR 500 confocal micro Raman spectrometer (Airix corp.) with the use of 532 nm laser source. Brunauer-Emmet-Teller (BET) surface area analysis was done by recording nitrogen adsorption/desorption isotherms at 77 K (BEL SORP II, Japan). Prior to the analysis samples were degassed at 200 °C in vacuum for 2 h. X-ray photoelectron spectroscopy (XPS) data were taken in the range of 1–1200 eV (Omicron Nanotechnology) to investigate the surface chemical composition of the PG sheets. AFM analysis was done by using SPM 9600 atomic force microscopy (Shimadzu) in tapping mode.

2.2.4. Electrochemical measurements

The working electrodes were made by mixing the active material PG, acetylene black and PVDF binder in a weight ratio of 8:1:1. Initially, active material and acetylene black were mechanically mixed together using a mortar and pestle and later a few drops of PVDF binder dissolved in NMP was added and mixed to get a slurry-like ink. The slurry-like ink was coated on one side of a Toray carbon paper of 2×2 cm^2 area using layer by layer brush coating technique. The coated carbon paper was heated at 60 °C for 8 h to reduce the effect of the binder used. The supercapacitor setup consisted of coated PG as working electrode material, 2 M KOH as an electrolyte, a filter paper soaked in the electrolyte as a separator and stainless-steel panels as current collectors [11,12]. The mass deposited on single carbon paper was found to be approximately equal to 3 mg. The electrochemical properties of single electrode were evaluated by coating the above stated slurry like ink on a Ni sheet of 1 cm^2 area using Doctor's blade technique followed by drying and employing a 3-electrode method. The mass deposited on the sheet was approximately 0.5 mg, as measured by a high precision weighing balance with a readability of 0.0001 g. Here, the coated Ni sheet served as the working electrode, saturated calomel as reference electrode, platinum wire as counter electrode. Cyclic voltammetry (CV), Galvanostatic charge-discharge (GCD), and electrochemical impedance spectra (EIS) analyses were performed using a computer controlled IVIUM electrochemical workstation. The specific capacitance values from the CV curves were calculated according to equation (1) [11,13].

$$C_S = \frac{nA}{\Delta V \times m \times \nu} \tag{1}$$

where C_s = specific capacitance (F g^{-1}), A is the integrated area of the CV curve, ΔV is the maximum potential window (V), m is the deposited mass on one single electrode (g), and ν is the scan rate (V s^{-1}). A factor of n = 2 is multiplied owing to the formation of series capacitance in a 2-electrode cell, for 3-electrode system, n = 1.

The specific capacitance values from the GCD curves were calculated using equation (2) [11,13].

$$C_s = n \times \frac{I \times \Delta t}{m \times \Delta V} \tag{2}$$

where C_s = specific capacitance (F g^{-1}), $\frac{I}{m}$ is the applied current density, Δt is the discharging time, ΔV is the maximum potential window to discharge the cell, n = 2 for 2-electrode system and n = 1 for 3-electrode system.

The energy density and power density of the prepared supercapacitor were calculated according to equations (3) and (4), respectively [14].

$$\text{Energy Density (Wh kg}^{-1}) = \frac{1}{2} C_s V^2 \tag{3}$$

$$\text{Power Density (W kg}^{-1}) = \frac{E}{t_d} \tag{4}$$

where, C_s = specific capacitance (F g^{-1}), V is the maximum potential window, E is the applied Energy density, t_d is the discharging time.

The specific capacity (mAh g^{-1}) values were also calculated from the CV data according to equation (5)

$$Q_s = C_s \times V \times 3.6 \tag{5}$$

where, C_s = specific capacitance (F g^{-1}), V is the maximum potential window.

2.2.5. Computational details

Electronic structure and density of states (DOS) calculations of pristine graphene and porous graphene were carried out within the framework of DFT using Quantum ESPRESSO package [15]. Ultrasoft scalar relativistic pseudopotentials with parametrized functional of Perdew, Burke and Erzenhoff were used to approximate the exchange-correlation energy functional [16]. The pseudopotential representing the ionic core implements a generalized gradient approximation considering $2s^2 2p^2$ as valence electrons of carbon. Fully relaxed supercells of $5 \times 5 \times 1$ and $10 \times 10 \times 1$ dimensions of primitive cell were used to simulate various pore concentrations. A vacuum layer of 12 Å was maintained to separate the adjacent periodic images of the sheet. K mesh of $9 \times 9 \times 1$ (for

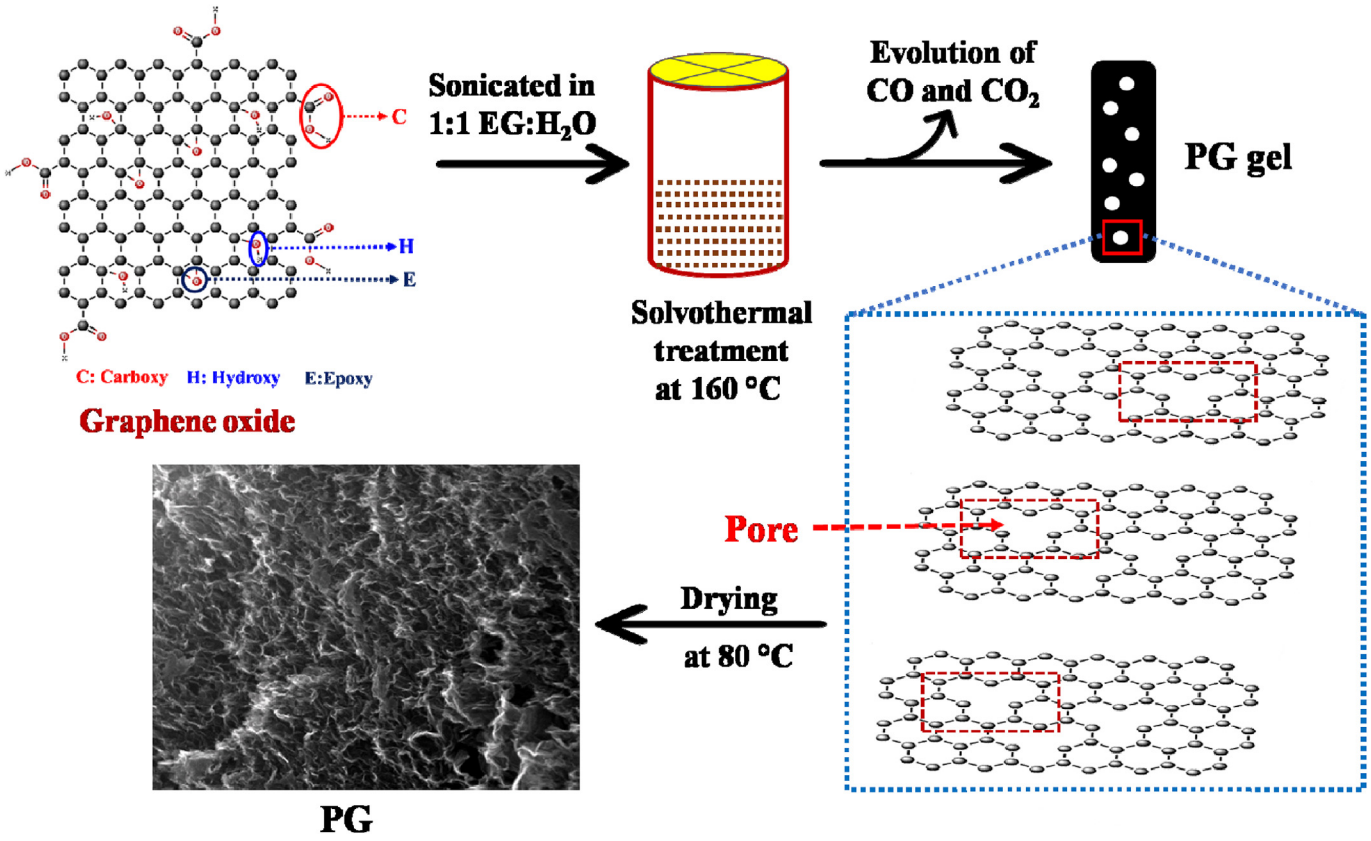

Scheme 1. Mechanism of formation of PG.

self consistent field calculations) and a denser grid of 36 × 36 × 1 (for obtaining DOS) were used to sample integrations over the Brillouin zone of the supercell. The electronic structure of the 2D sheet was determined along Γ - M - K - Γ high symmetry path. Electronic wave functions represented by plane wave basis set were truncated with an energy cutoff of 50 Ry and charge density with a cutoff of 400 Ry.

3. Results and discussion

3.1. Structural and morphological analysis

Fig. 1 shows the XRD patterns of the synthesized GO and PGs. In GO there is a characteristic peak at 9.4° corresponding to the (001) crystal planes. The interlayer spacing of the GO is around 0.94 nm as compared to the pristine graphite of 0.34 nm, which clearly indicates that the high degree of oxygenation has occurred in the sample. In PG, the (001) crystal planes disappear and new peaks are observed at 20–25° and 40–45° range, which correspond to the characteristic (002) and (100) planes of the graphene respectively [17].

The calculated d-spacings from the Bragg's law is given in Table 1 and the d-spacings are close to the value of graphite i.e.; 0.34 nm calculated from the XRD peak of graphite (Fig. S1) depicting the restoration of the graphite moiety. The XRD peaks of the PG are broad in nature, suggesting the stacked nature of the sheets and thickness of few layers. From the XRD peaks and Scherrer equation, the average number of layers was calculated using equation (6) [18].

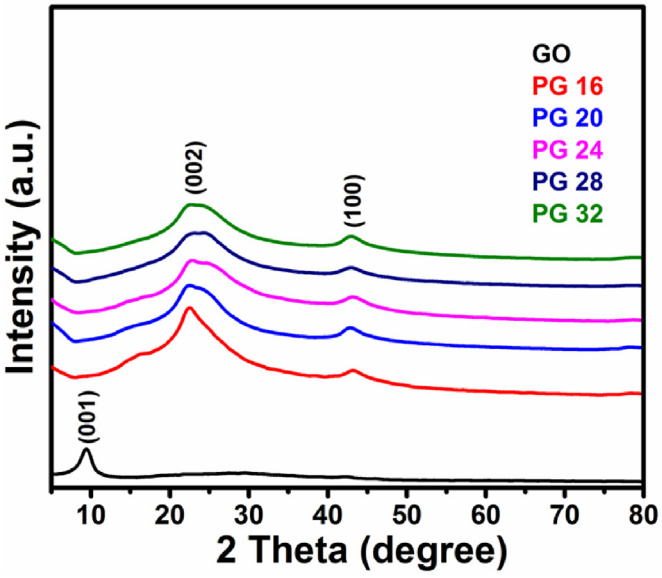

Fig. 1. XRD patterns of the prepared GO and PG samples.

$$N = \frac{L}{d} + 1 \quad (6)$$

where N is the number of layers, L is the crystallite size obtained from Scherrer equation and d is the d-spacing between the planes. The number of layers calculated using the formula was found to be

Table 1
2θ values and their corresponding d-spacing values for synthesized GO and PG.

Sample name	2θ values (°)	d-spacing (nm)
GO	9.40	0.94
PG 16	22.42	0.396
PG 20	22.90	0.388
PG 24	23.00	0.386
PG 28	23.61	0.376
PG 32	22.53	0.394

~4–6.

Fig. 2a shows the FESEM image of the PG sheets, showing the crumpled and wrinkled structure indicating the soft, flexible and porous morphology and stacked nature consistent with XRD results. The SEM and TEM image of GO are shown in Fig. S2.

In order to confirm the generation of pores on the sheets, 0.05 mg PG sample was dispersed in 5 mL of ethanol and ultrasonicated for 2 min and one drop of this dispersion was drop casted on to the carbon sheet and was vacuum dried in order to remove the solvent. The TEM image revealing the porous nature and SAED pattern of PG sheet is shown in Fig. 2b. The EDX pattern is given in Fig. S3 showing only C and O as elements present.

Raman spectroscopy is a potent technique to characterize the graphene samples in terms of crystal disorders, defects, and hybridization [9]. The Raman spectra of GO and PG samples are shown in Fig. 3. In all the samples the D band (formed due to the breathing mode of κ-point phonons of A_{1g} symmetry) and G band (formed due to the first order scattering of the E_{2g} mode) are present confirming the defect formation and restoration of graphite moiety in the PG samples [19].

In the Raman spectra of graphite used for synthesis (Fig. S4), there is presence of D, G and 2D bands at 1353.4, 1580 and 2710 cm^{-1} respectively. The very low intensity of D band indicates lesser number of defects in graphite samples. After the onset of reduction process, the progressive increase in the intensity of the D band, the broadening of G band and blue shifting of the peak from 1580 cm^{-1} for GO to 1590–1599 cm^{-1} for PG samples indicate the formation of defects and decrease in number of layers in the samples [19]. For a better view, magnified display of Raman shift of the D and G bands is shown in Fig. S5. The relative intensity ratio (I_D/I_G) of the D and G bands is a measure of the defects formed in the sample and is inversely proportional to the average size of the sp^2 domains [17]. The calculated (I_D/I_G) values for GO and PG samples are tabulated in Table 2.

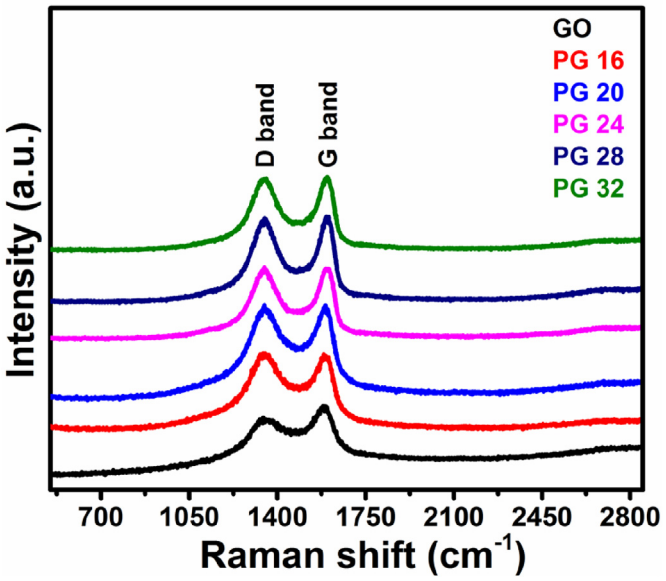

Fig. 3. Raman spectra of GO and PG samples showing D and G bands.

Table 2
D and G band positions and their corresponding I_D/I_G ratio values for GO and PG.

Sample name	D band position	G band position	I_D/I_G ratio
GO	1351.0	1580.0	0.76
PG 16	1347.4	1590.0	0.94
PG 20	1347.4	1590.0	1.01
PG 24	1351.0	1594.0	1.07
PG 28	1351.0	1599.0	1.10
PG 32	1347.4	1594.8	1.05

Analysis of values in Tables 1 and 2 reveals that there is an inverse trend in the D and G band positions of Raman spectrum and XRD traces of PG 32 sample. This may be explained as follows: Compared to other samples, PG 32 was formed with a reaction time of 32 h. This larger duration of reaction can cause better exfoliation and hence increased distance between planes of graphene crystallite. Accordingly, XRD trace of this sample showed higher d-spacing and reduction in the 2-theta value. Due to the same reason, the sample undergoes better reduction and possesses lesser extent of defects. This will result in lower value of D-band in Raman

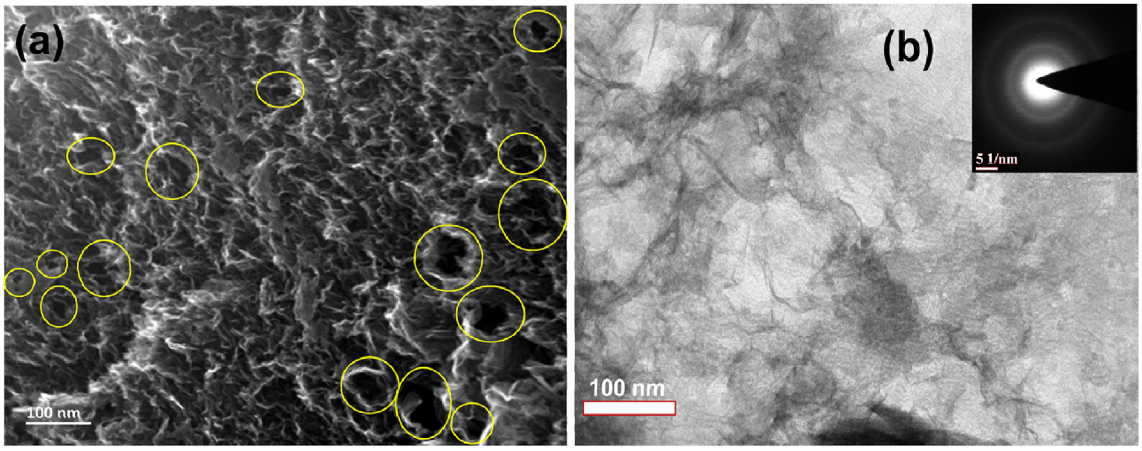

Fig. 2. FESEM image of (a) PG sheets, (b) TEM image of the PG sheet showing numerous pores on the sheet (inset shows the SAED pattern of PG).

spectrum. However, the variation of these values is not regular or linear and there can also be several other reasons contributing to these effects. More detailed studies are needed to understand this behavior and to make any conclusive remarks on this trend.

The surface area is an important parameter for PG. All the prepared samples were analyzed for their surface area. Fig. 4a shows the N_2 adsorption-desorption isotherm of the PG samples, which conform to the characteristic type-IV isotherm with hysteresis loop in the P/P° range of 0.4–1.0. These results suggest the presence of mesopores in the samples. The calculated surface areas of the samples by using the BET method were found to be 126, 185, 269, 420 and 338 $m^2 g^{-1}$ for PG 16, PG 20, PG 24, PG 28 and PG 32 respectively. Among the tested samples, PG 28 exhibited highest surface area as well as good restoration of graphitic moiety as indicated by the G band intensity in the Raman spectrum. These features contribute to high charge storage and transportation characteristics. In view of this, the PG 28 sample has been selected as the best sample for electrochemical characterizations. A comparison of the surface area of the PG materials reported in the literature is given in Table S1.

The pore size analysis of the PG 28 sample has also been done and is shown in Fig. 4b. As can be seen from the plot, the sample possesses hierarchical porous structure with pores of microporous (1.7 nm) and mesoporous (3.5 and 9.8 nm) nature. The creation of hierarchical porous structure at high temperatures is in accordance with the literature [20]. Such hierarchical porous structure and high surface area of the sample help higher charge storage and thereby increases the capacitance value [21].

AFM analysis was carried out in order to know the surface topography of the PG sample. The 3D image shown in Fig. 5a shows some deep cavities which corroborates the porous nature of the sample. The 2D topographic image shown in Fig. 5b shows some voids/pits in the plane which confirms the porous nature of the material. The topographic image of one selected area and its corresponding measured height profile is represented in Fig. 5c and d. The topographic images confirm the successful synthesis of the PG.

The chemical composition of the PG 28 sample was analyzed by XPS technique. The survey spectrum of the PG 28 sample is shown in Fig. S6, wherein only carbon (87.7 at. %) and oxygen (12.3 at. %) were present suggesting the high purity of the sample. The low content of the oxygen in the sample indicates that appreciable reduction has occurred in the PG 28 sample. The deconvoluted C 1s spectra (Fig. 6a) shows the existence of a sharp peak at 284.5 with a flat tail towards higher binding energy, depicting the restoration of sp^2 moiety in the sample [22]. The peaks at binding energies of 285.9 and 288.5 eV correspond to the C–O and C=O species, respectively in the sample [23,24]. The deconvoluted O 1s spectra (Fig. 6b) reveals two peaks at binding energies of 531.2 and 532.8 eV which may be ascribed to the C=O and C–O species, respectively [19,25].

3.2. Role of solvent mixture in the reduction of GO to PG

It is known that solvothermal reduction of GO proceeds in two stages: 1) Partial reduction that depends on the solvent polarity and 2) Further reduction to fully restore sp^2 structure of graphene. This second stage is strongly depending on solvent surface energy which controls the agglomeration of partially reduced GO. The solvent which can keep the GO well dispersed is believed to facilitate efficient reduction and thus the reduction of GO is highly susceptible to surface energy of solvents [26]. It has been derived through appropriate theoretical considerations that for maintaining such good dispersal of GO, surface energy of the solvent should be in the range of 70–80 mJ/m^2 or slightly higher [27]. In our study, we have employed ethylene glycol-water binary mixture for the reduction of GO by solvothermal approach. The surface tension of water and ethylene glycol were calculated using equations (7) and (8), respectively.

$$\gamma = B\left(\frac{T_c - T}{T_c}\right)^{\mu}\left[1 + b\left(\frac{T_c - T}{T_c}\right)\right] \tag{7}$$

$$\gamma = \gamma_o\left(1 - \frac{T}{T_c}\right)^{n} \tag{8}$$

where, $B = 235.8 \times 10^{-3}$ N/m, $b = -0.625$, $\mu = 1.256$, T is the temperature of the solvent, T_c is the critical temperature, n is an empirical factor which is equal to 11/9 for organic liquids and γ_o is a constant for each liquid which is given in equation (9).

$$\gamma_o = \frac{kT_c}{V^{2/3}} \tag{9}$$

where k is a universal constant (2.1×10^{-7}), V is the molar volume of the liquid and T_c is the critical temperature of the liquid. For ethylene glycol the value of γ_o was found to be 1.5135 J/m^2. The

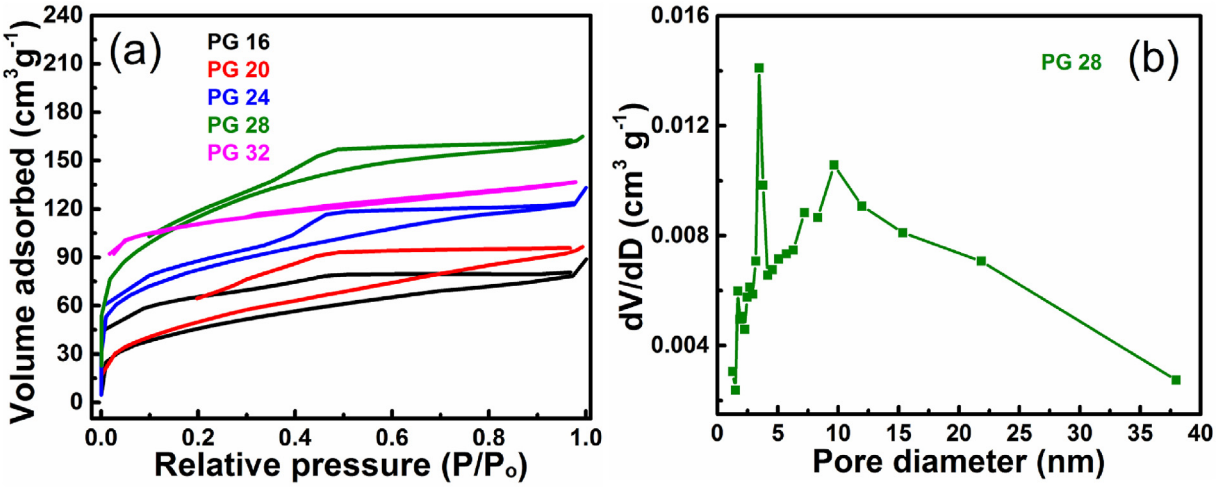

Fig. 4. (a) BET surface area, (b) pore size distribution of PG 28.

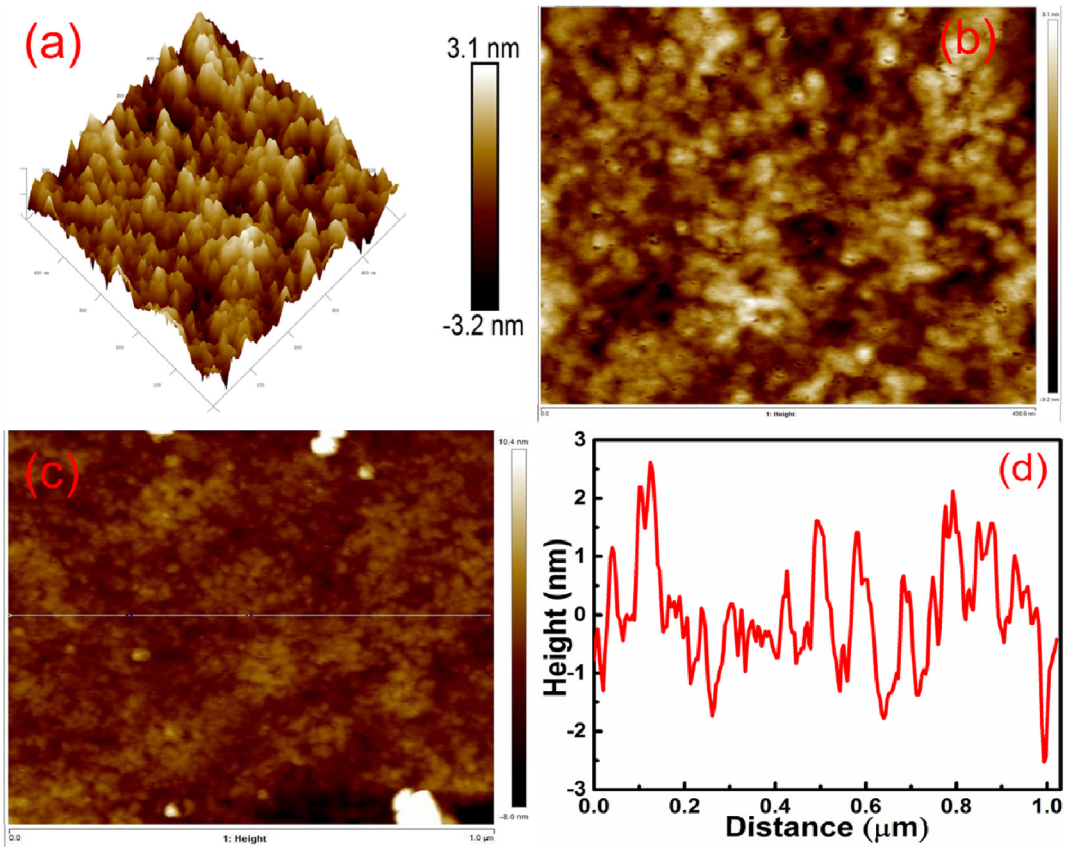

Fig. 5. AFM image of PG 28 (a) 3D image, (b) 2D image showing the formation of pores, (c) topographic image and (d) height profile of the PG 28 corresponding to the white line drawn in (c). The value of Ra is 0.9 nm and Rq is 1.2 nm.

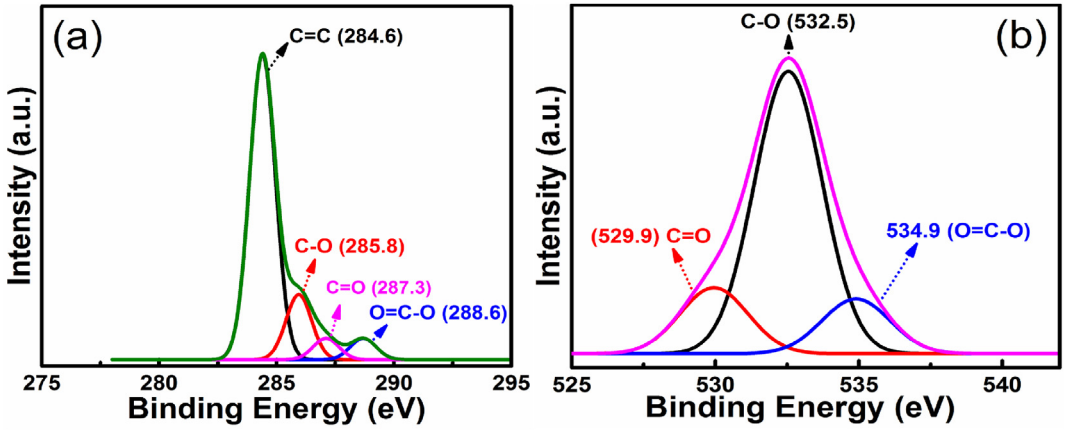

Fig. 6. XPS data of PG 28 (a) deconvoluted C 1s and (b) deconvoluted O 1s spectra.

calculated surface tension values for water and ethylene glycol at our solvothermal condition of 433 K are 46.5 mJ/m^2 and 21.6 mJ/m^2 respectively. For a solution of an organic compound (here ethylene glycol) and water, the surface tension can be expressed as in equation (10) [28,29].

$$\gamma_{mixing} = x.\ \gamma_{ethylene\ glycol} + y.\ \gamma_{water} \quad (10)$$

where, x and y represent the mole fractions of ethylene glycol and water, respectively. In our experiment the surface tension of binary mixture (equal volumes of ethylene glycol and water) was found to be 40.4 mJ/m^2 at 433 K. The surface energy can be calculated from surface tension values and the same for pure water, pure ethylene glycol and binary mixture are 89.8, 65.0 and 79.4 mJ/m^2, respectively. Hence, it is evident that the surface energy of water is on the higher side and that of ethylene glycol is on the lower side of required range for an efficient reduction process, whereas the surface energy of the solvent mixture we used falls in the required range. Thus, the binary solvent mixture that we used is supposed to facilitate efficient reduction of GO under the employed solvothermal condition.

Further, under the prevailing conditions, the oxygen containing

groups such as; carboxylic, carbonyl, and hydroxyl groups are believed to decompose into CO or CO_2 which can be entrapped into the hydrogel leading to the formation of the pores. Also, the overlapping and coalescence of graphene sheets can lead to the formation of pores in the resulting reduced graphene sheets, as reported previously [30,31].

3.3. Electronic structure analysis by DFT

For graphene based supercapacitors, the total capacitance is the resultant of double layer capacitance and quantum capacitance as though they were combined in series [32]. Graphene has a large surface area due to which it can accommodate electrolyte ions and in turn increase the double layer capacitance. Hence, the limiting factor is the finite quantum capacitance which is dependent on the electronic structure [33,34]. The optimized structure of pristine graphene is a 2D sheet with carbon atom forming hexagonal rings with C–C bond length of 1.42 Å consistent with the previous reports [32,34]. The electronic structure of pristine graphene reveals a zero band gap at K point (Dirac point) with no states visible near the Fermi level in the DOS plot indicative of the vanishing gap (Fig. 7a). The major drawback of pristine graphene in supercapacitor application is the low quantum capacitance which is a direct consequence of lack of states near the Fermi level [33,34]. To simulate various defect concentration $10 \times 10 \times 1$ supercell with a single pore arising out of missing carbon atom (Fig. S7); $5 \times 5 \times 1$ supercells with one and two pores were considered. The carbon atoms closer to the vacancy appear strained with C–C bond distance of 1.39 Å while the carbon atoms further away from the pore do not exhibit any such strain (C–C bond distance remains ~1.42 Å).

Fig. 7b reveals the appearance of a defect band, lying 0.035 eV above the valence band maximum (VBM) at K point and 0.084 eV below the conduction band minimum (CBM). The density of states shows a prominent sharp peak exactly at the Fermi level due to the flat defect band. The partial density of states reveals that the carbon atoms in close vicinity of the point defect (shown in darker color in Fig. S7) is responsible for the increase in DOS near the Fermi level as the electronic structure becomes more localized in the area near the defect. The states formed have major contribution from the 'p' orbitals and minor contribution from 's' orbitals (Fig. S8). It is believed that flatter bands and creation of higher density of states near the Fermi level leads to greater amount of accumulation of electrical charges there by increasing the supercapacitance of the material as quantum capacitance is directly proportional to the DOS around the Fermi level [32,34]. The electronic structure of a $5 \times 5 \times 1$ supercell with a single pore reveals opening of the band gap with the mid gap defect level with a width of 0.399 eV, appearing 0.644 eV (K → M-δ′) above the VBM and 0.369 eV below the CBM (at K point). This appears as an asymmetric peak in the DOS plot (Fig. 7c). When the number of pores is further increased to 2 per sheet, the mid gap defect level disappears and the bands introduced by the carbon atoms closer to the missing carbon atom appears just beneath the CBM overlapping with it (Fig. 7d). An indirect band gap (K+δ → M) of 1.156 eV is observed. The abundant

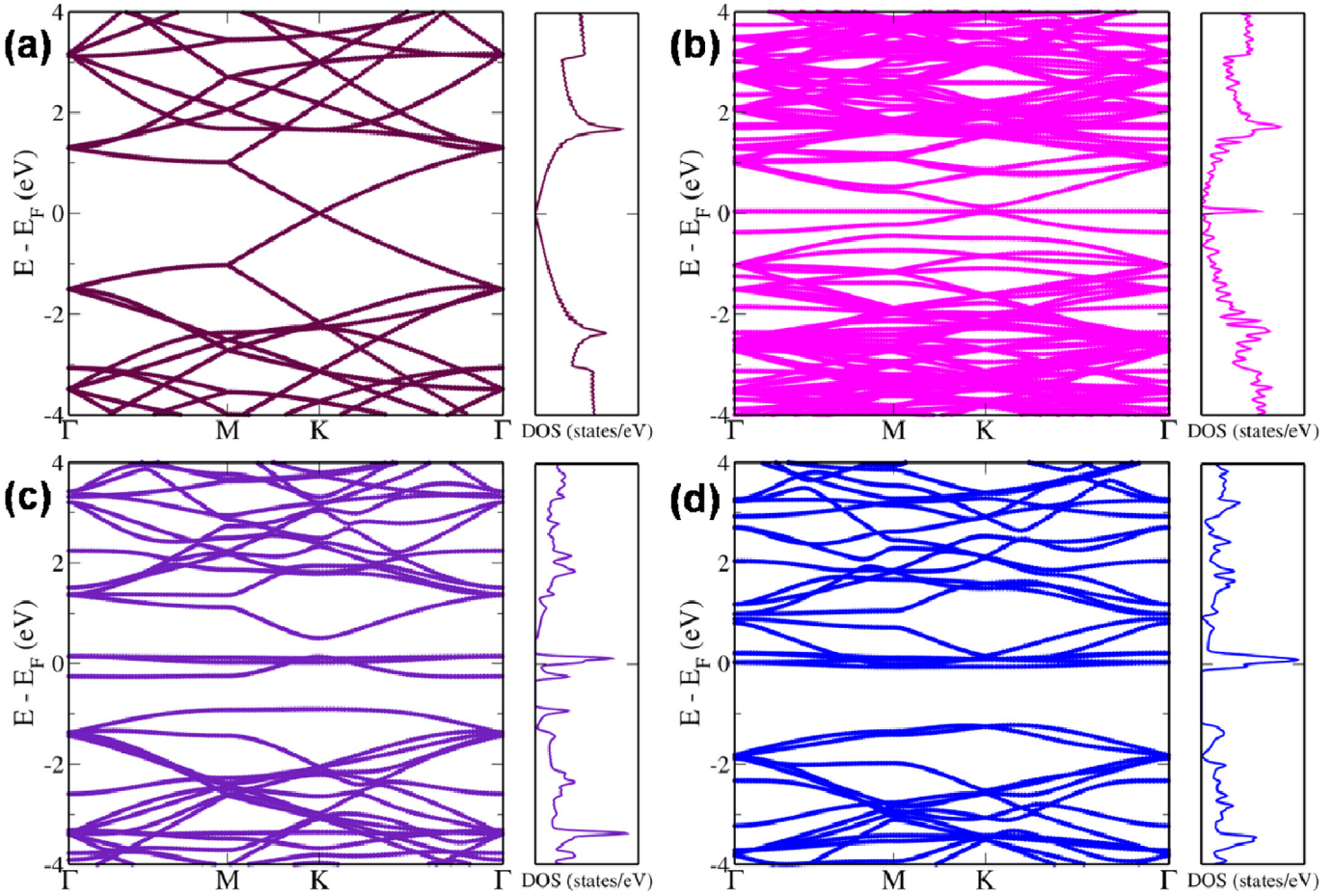

Fig. 7. Electronic structure and DOS of a) pristine graphene; b) $10 \times 10 \times 1$ supercell of porous graphene with a single pore; c) $5 \times 5 \times 1$ supercell of porous graphene with a single pore; d) $5 \times 5 \times 1$ supercell of porous graphene with double pores. The energies are shifted with respect to Fermi level which is set to zero.

states near the Fermi level and widened band gap increases the capacitance of the PG sheet improving its supercapacitor performance [34]. Thus, the high surface area of PG 28 sample leads to high double layer capacitance and the tuning of electronic structure and DOS due to the formation of large number of pores enhances its quantum capacitance and in turn the combined effect leads to high specific capacitance of the material.

3.4. Electrochemical measurements

The electrochemical performance of the PG 28 sample was studied by a conventional 3 electrode method by using 2 M KOH as electrolyte employing CV, GCD and EIS. The electrochemical characterization was done in both negative and positive potential range. Fig. 8a shows the CV curves at scan rates ranging from 5 to 200 mV s^{-1} in the potential range −0.6 V to 0.2 V. The obtained CV curves are nearly rectangular in shape suggesting the EDLC behavior of the sample. The calculated specific capacitance values calculated following equation (1) are, 484, 473, 412, 356, 267, 156 and 85 F g^{-1} for the scan rates 5, 10, 20, 30, 50, 100 and 200 mV s^{-1}, respectively.

The GCD curves at different current densities ranging from 1 to 12 A g^{-1} are shown in Fig. 8b. The symmetrical nature of charge-discharge curves is suggestive of the good electrochemical trait of the material. The calculated specific capacitance values from the GCD data as per equation (2) are 437, 380, 326, 250, 232, 220, and 158, and 128 F g^{-1} for the current densities of 1, 1.5, 2, 2.5, 3, 4, 5, and 6 A g^{-1}, respectively. The Nyquist plot of the PG 28 sample is displayed in Fig. 8c. The high frequency region is shown as an inset displaying the lower arc part of the plot. The very small semicircle at high frequency region and flat tail parallel to the Y-axis in the low frequency region are characteristic of good capacitive property of the material. The fitted equivalent circuit is also shown as an inset of Fig. 8c. As can be seen from the figure, the fitted plot is well matched with the experimental plot, confirming the validity of the determined equivalent circuit [35].

The admittance plot for PG 28 is shown in the inset of Fig. 8c. Knee frequency for the material can be determined from this plot. From the knee frequency value, the relaxation time constant can be obtained. Above the knee frequency the capacitor would be resistive in nature. Hence, the capacitor would be more useful below this knee frequency. The calculated knee frequency for the present material is 25.1 kHz and the corresponding time constant value is 39.8 μs. The result indicates that the material would be an efficient capacitor for a good range of frequency. The cyclic stability study is an important parameter as for as practical application of the supercapacitor. Hence, we tested the PG 28 sample for 10000 cycles at a constant scan rate of 100 mV s^{-1} (Fig. 8d). The test showed retention of 87% of the initial capacitance value even after 10000 cycles, suggesting the good stability of the material. The good performance executed by the material is mainly attributed to the porous nature of the sample. Further, the material exhibited a maximum energy density of 34.2 Wh kg^{-1} and a maximum power density of 2400 W kg^{-1} in the studied range of current density

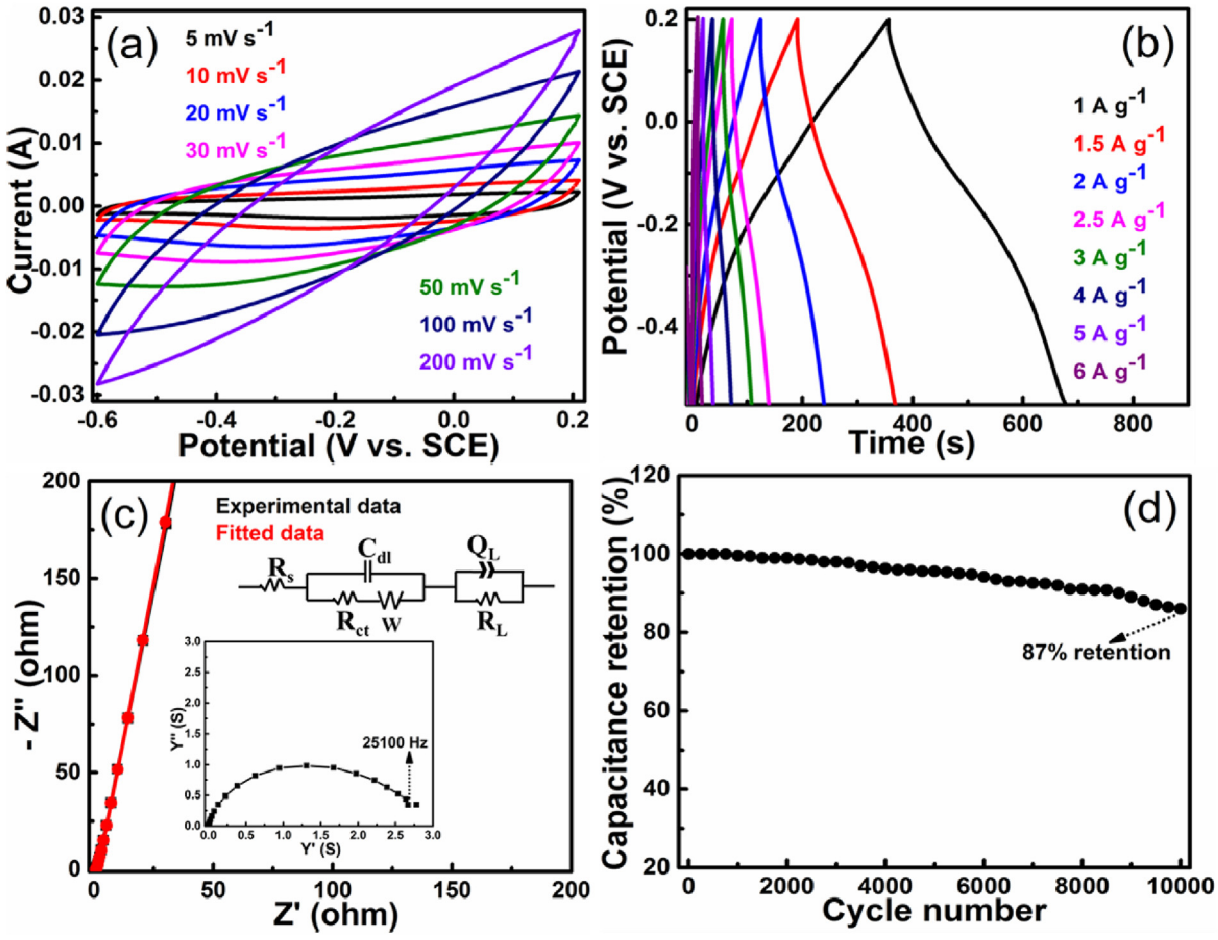

Fig. 8. Electrochemical results of PG 28 in the negative potential range. (a) CV curves at various scan rates, (b) GCD curves at various current densities, (c) Nyquist plot: high frequency region and equivalent circuit as insets and (d) Cyclic stability test at a scan rate of 100 mV s^{-1} for 10000 cycles.

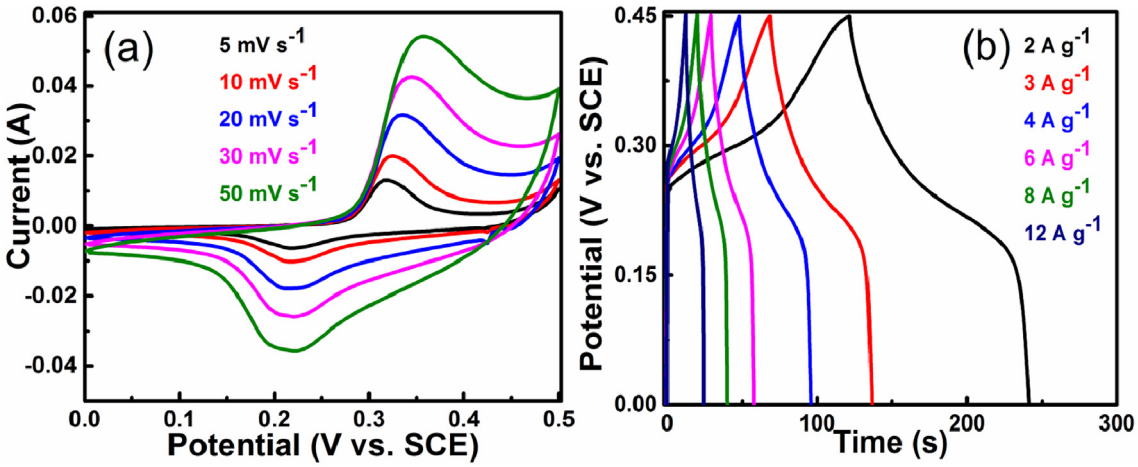

Fig. 9. Electrochemical results of PG 28 in positive potential range (0–0.5 V) (a) CV curves at various scan rates and (b) GCD curves at various current densities.

(Table S2).

The electrochemical analysis of PG 28 sample in the positive potential range of 0 V–0.5 V is shown in Fig. 9. The CV curves at various scan rates ranging from 5 to 50 mV s^{-1} is displayed in Fig. 9a. It is evident from the nature of the CV curves that they show pseudocapacitive trait in the positive potential. The pair of redox peaks observed here is due to the presence of oxygen functionalities present in PG sample as it is not completely reduced. They show redox reactivity in the positive potential range. Such results have also been reported in the literature [36,37]. For example, Oyedotun et al. (2017) have reported such kind of CV pattern for carbon nanorods in the positive potential range of 0–0.4 V [36]. The calculated specific capacitance values for the PG 28 material are, 666, 581, 556, 542, and 457 F g^{-1} at the scan rates of 5, 10, 20, 30, and 50 mV s^{-1}, respectively.

The GCD curves at different current densities ranging from 2 to 12 A g^{-1} are presented in Fig. 9b. The charge-discharge curves are also showing pseudocapacitive characteristics like that in the CV curves. The calculated specific capacitance values from the GCD data are, 567, 501, 480, 427, 392, and 373 F g^{-1} for the current densities of 2, 3, 4, 6, 8 and 12 A g^{-1}, respectively. The calculated maximum energy density and maximum power density of the material from this GCD data in the studied range of current density are 15.9 Wh kg^{-1} and 2569.2 W kg^{-1} respectively. (Table S3).

Further, to evaluate the contribution of blank electrode to the specific capacitance value of the material in both negative and positive potential windows, we measured the CVs for blank electrode and the blank electrode coated with the active material (Fig. 10). The results very clearly demonstrate that the contribution from the blank electrode in both the potential windows is negligible.

The electrochemical performance of the fabricated symmetrical supercapacitor employing PG 28 electrodes is presented in Fig. 11. The CV curves at various scan rates ranging from 5 to 200 mV s^{-1} are displayed in Fig. 11a. The obtained CV curves are nearly rectangular in shape suggesting the EDLC behavior of the sample. The calculated specific capacitance values are, 297, 259, 207, 179, 145, 122, and 73 F g^{-1} for the scan rates 5, 10, 20, 30, 50, 100, and 200 mV s^{-1}, respectively. The GCD curves at different current densities ranging from 1.5 to 6 A g^{-1} is shown in Fig. 11b. The near symmetrical charge-discharge curves are an indication of good electrochemical performance of the material. The calculated specific capacitance values are 189, 121, 110, 80, 77, 70, and 61 F g^{-1} for the current densities of 1.5, 2, 2.5, 3, 4, 5, and 6 A g^{-1}, respectively. The calculated maximum energy density and maximum power density of the material from this GCD data in the studied range of current density are, 26.3 Wh kg^{-1} and 6120.0 W kg^{-1}, respectively. (Table S4).

Fig. 11c shows the Nyquist plot of the PG 28 sample. The high frequency region shows a semicircle and an inclined line in the low frequency region. The lower radius of the semicircle depicts the low resistance and high capacitive nature of the PG 28 active material.

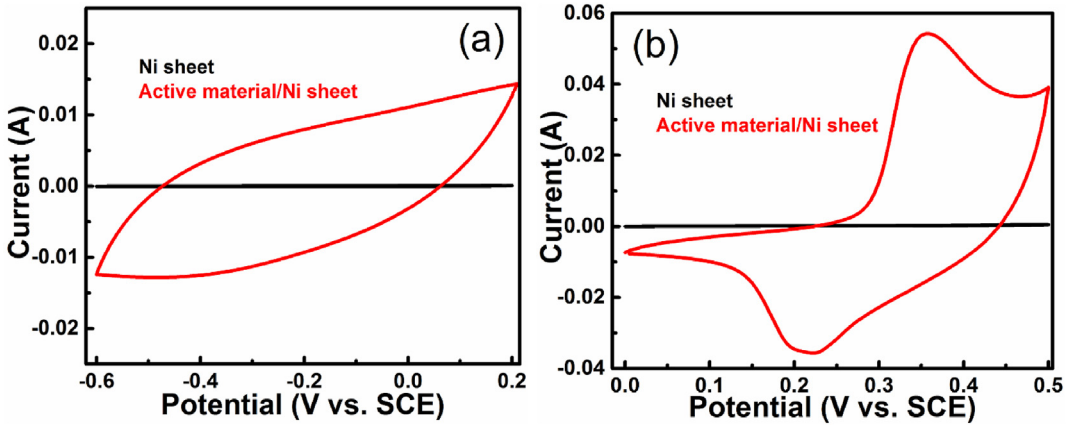

Fig. 10. CVs of bare Ni sheet and PG 28 coated Ni sheet in (a) negative and (b) positive potential windows at a constant scan rate of 50 mV s^{-1}.

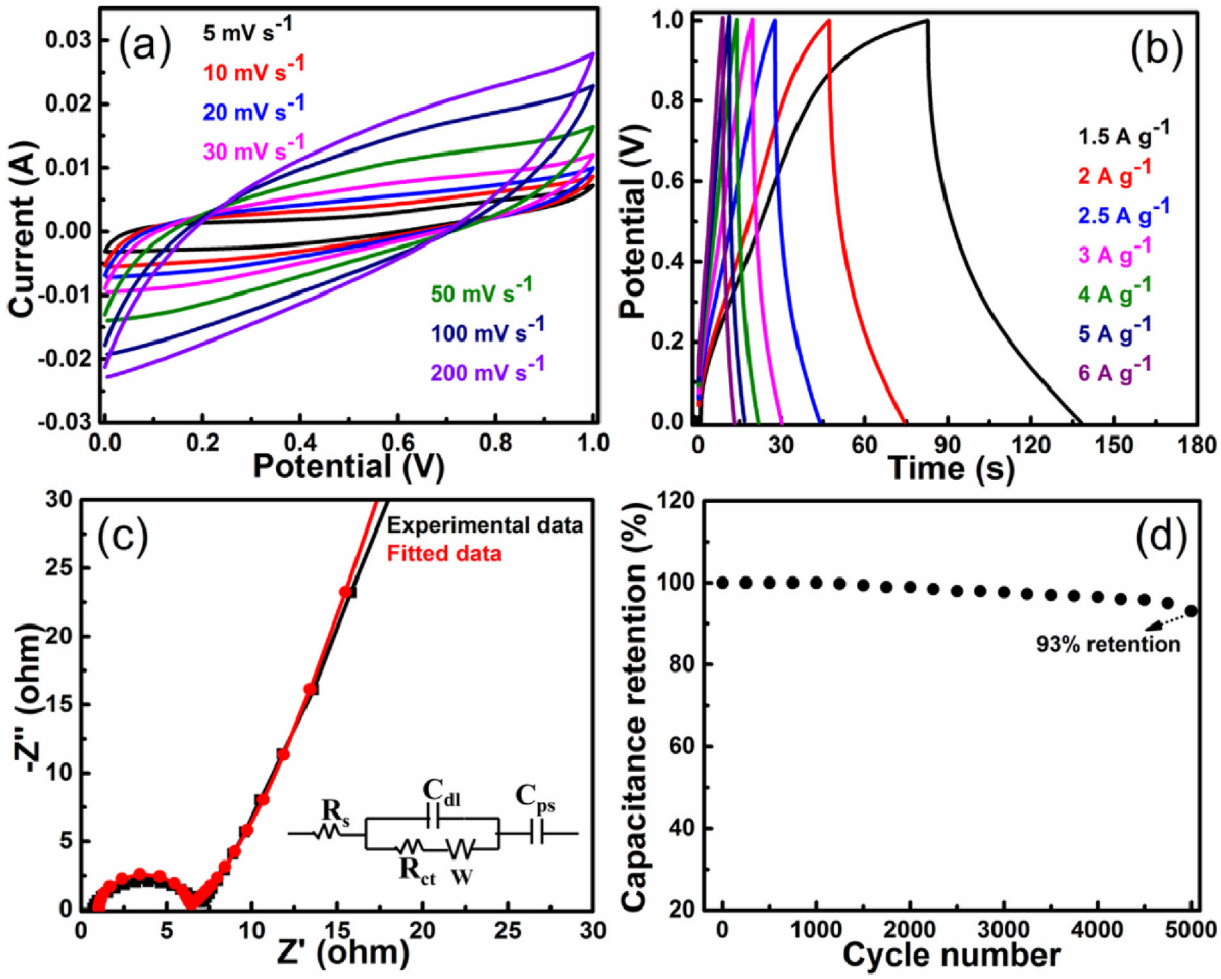

Fig. 11. Electrochemical results of symmetrical supercapacitor fabricated from PG 28 electrodes. (a) CV curves at various scan rates, (b) GCD curves at various current densities, (c) Nyquist plot inset: equivalent circuit and (d) cyclic stability test at a scan rate of 100 mV s^{-1} for 5000 cycles.

The inset in Fig. 11c shows the fitted equivalent circuit determined according to the Randle equivalent circuit fitting method [38]. The fabricated supercapacitor is tested for its stability by cycling tests (Fig. 11d). It is evident from the figure that the supercapacitor has retained 93% of the initial capacitance value even after 5000 cycles, indicating a fairly high stability of the material. The good performance executed by the material is mainly attributed to the porous nature of the sample. We have compared the specific capacitance values of PG 28 material with those of the recently reported in the literature (Table S5). We can see from the Table that our material exhibits highest capacitance amongst all other materials and it also has a merit of being synthesized using an eco-friendly and facile method.

4. Conclusion

In summary, we report here a greener approach for the synthesis of PG samples without addition of any toxic reducing agents and employing a 1:1 binary mixture of ethylene glycol and water as solvent in a solvothermal approach. The samples were thoroughly analyzed for the structural, morphological and elemental compositions. Morphological analysis revealed the formation of porous structure on the surface of the sheets. Among the synthesized PG samples, PG 28 showed a high surface area of 420 $m^2 g^{-1}$ with hierarchical porous structure and mean pore diameter of 3.4 nm according to BET analysis. The DFT calculations showed that the introduction of defects in the form of pores led to the increase in the DOS near the Fermi level due to introduction of 2p states of the carbon atoms in the close vicinity of the vacancy defects leading to the increase in the capacitance value. The PG 28 sample exhibited an impressive high capacitance value of 666 F g^{-1} at a scan rate of 5 mV s^{-1} in the positive potential range of 0–0.5 V. The symmetrical supercapacitor fabricated using the PG 28 electrodes retained 93% of its initial capacitance value even after 5000 cycles of charge -discharge process and exhibited a maximum energy density of 26.3 Wh kg^{-1} and maximum power density of 6120 W kg^{-1} in the studied current density range. The impressive result shown by the material is mainly due to the high surface area of the sample with hierarchical porous structure which not only provided the open channels but also provided the conductive path for the efficient charge storage and transport of ions.

Acknowledgements

MS is grateful to the National Institute of Technology Karnataka, Surathkal, Mangalore, for providing financial support in the form of an Institute fellowship.

Appendix A. Supplementary data

Supplementary data to this article can be found online at https://doi.org/10.1016/j.jallcom.2019.05.302.

References

[1] B.D. Zdravkov, J.J. Čermák, M. Šefara, J. Janků, Pore classification in the characterization of porous materials: a perspective, Cent. Eur. J. Chem. 5 (2007) 385–395.

[2] P. Russo, A. Hu, G. Compagnini, Synthesis, properties and potential applications of porous graphene: a review, Nano-Micro Lett. 5 (2013) 260–273.

[3] K. Ghosh, C.Y. Yue, M.M. Sk, R.K. Jena, S. Bi, Development of a 3D graphene aerogel and 3D porous graphene/MnO_2@polyaniline hybrid film for all-solid-state flexible asymmetric supercapacitors, Sustain. Energy Fuels 2 (2018) 280–293.

[4] X. Meng, L. Lu, C. Sun, Green synthesis of three-dimensional MnO_2/graphene hydrogel composites as a high-performance electrode material for supercapacitors, ACS Appl. Mater. Interfaces 10 (2018) 16474–16481.

[5] X. Liu, S. Zou, K. Liu, C. Lv, Z. Wu, Y. Yin, T. Liang, Z. Xie, Highly compressible three-dimensional graphene hydrogel for foldable all-solid-state supercapacitor, J. Power Sources 384 (2018) 214–222.

[6] H.G. Kang, J.M. eong, S.B. Hong, G.Y. Lee, J.W. Kim, B.G. Choi, Scalable exfoliation and activation of graphite into porous graphene using microwaves for high–performance supercapacitors, J. Alloys Compd. 770 (2019) 458–465.

[7] Y. Chai, Z. Li, J. Wang, Z. Mo, S. Yang, Construction of hierarchical holey graphene/MnO_2 composites as potential electrode materials for supercapacitors, J. Alloys Compd. 775 (2019) 1206–1212.

[8] Y. Bai, Z. Yan, L. Kang, Z.H. Liu, Preparation and capacitance of V_2O_5/holey graphene hybrid aerogel electrode with high performance, J. Alloys Compd. 780 (2019) 792–799.

[9] M.M.J. Sadiq, U.S. Shenoy, D.K. Bhat, Synthesis of BaWO4/NRGO-g-C3N4 nanocomposites with excellent multifunctional catalytic performance via microwave approach, Front. Mater. Sci. 12 (2018) 247–263.

[10] D.C. Marcano, D.V. Kosynkin, J.M. Berlin, A. Sinitskii, Z. Sun, A. Slesarev, L.B. Alemany, W. Lu, J.M. Tour, Improved synthesis of graphene oxide, ACS Nano 4 (2010) 4806–4814.

[11] A.K. Mishra, S. Ramaprabhu, Functionalized graphene-based nanocomposites for supercapacitor application, J. Phys. Chem. C 115 (2011) 14006–14013.

[12] B. Subramanya, D.K. Bhat, Novel one-pot green synthesis of graphene in aqueous medium under microwave irradiation using a regenerative catalyst and the study of its electrochemical properties, New J. Chem. 39 (2015) 420–430.

[13] H. Feng, P. Xie, S. Xue, L. Li, X. Hou, Z. Liu, D. Wu, L. Wang, P.K. Chu, Synthesis of three-dimensional porous reduced graphene oxide hydrogel/carbon dots for high-performance supercapacitor, J. Electroanal. Chem. 808 (2018) 321–328.

[14] M. Sethi, D.K. Bhat, Facile solvothermal synthesis and high supercapacitor performance of $NiCo_2O_4$ nanorods, J. Alloys Compd. 781 (2019) 1013–1020.

[15] P. Giannozzi, S. Baroni, N. Bonini, M. Calandra, R. Car, C. Cavazzoni, D. Ceresoli, G.L. Chiarotti, M. Cococcioni, I. Dabo, et al., Quantum Espresso: a modular and open-source software project for quantum simulations of materials, J. Phys. Condens. Matter 21 (2009) 395502.

[16] J.P. Perdew, K. Burke, M. Ernzerhof, Generalized gradient approximation made simple, Phys. Rev. Lett. 77 (1996) 3865–3868.

[17] M.M.J. Sadiq, S. Mutyala, J. Mathiyarasu, D.K. Bhat, RGO/$ZnWO_4$/Fe_3O_4 nanocomposite as an efficient electrocatalyst for oxygen reduction reaction, J. Electroanal. Chem. 799 (2018) 102–110.

[18] B. Subramanya, D.K. Bhat, Novel eco-friendly synthesis of graphene directly from graphite using 2, 2, 6, 6-tetramethylpiperidine 1-oxyl and study of its electrochemical properties, J. Power Sources 275 (2015) 90–98.

[19] M.M.J. Sadiq, U.S. Shenoy, D.K. Bhat, Enhanced photocatalytic performance of N-doped RGO-$FeWO_4$/Fe_3O_4 ternary nanocomposite in environmental applications, Mater. Today Chem. 4 (2017) 133–141.

[20] M.J. Illán-Gómez, A. Garcia-Garcia, C. Salinas-Martinez de Lecea, A. Linares-Solano, Activated carbons from Spanish coals. 2. chemical activation, Energy Fuels 10 (1996) 1108–1114.

[21] M. Sevilla, R. Mokaya, A.B. Fuertes, Ultrahigh surface area polypyrrole-based carbons with superior performance for hydrogen storage, Energy Environ. Sci. 4 (2011) 2930–2936.

[22] M.M.J. Sadiq, U.S. Shenoy, D.K. Bhat, $NiWO_4$-ZnO-NRGO ternary nanocomposite as an efficient photocatalyst for degradation of methylene blue and reduction of 4-nitro phenol, J. Phys. Chem. Solids 109 (2017) 124–133.

[23] M. Srivastava, M.E. Uddin, J. Singh, N.H. Kim, J.H. Lee, Preparation and characterization of self-assembled layer by layer $NiCo_2O_4$–reduced graphene oxide nanocomposite with improved electrocatalytic properties, J. Alloys Compd. 590 (2014) 266–276.

[24] M.M.J. Sadiq, U.S. Shenoy, D.K. Bhat, High performance bifunctional catalytic activity of novel zinc tungstate–reduced graphene oxide nanocomposite, Adv. Sci. Eng. Med. 9 (2017) 115–121.

[25] M.M.J. Sadiq, U.S. Shenoy, D.K. Bhat, Novel RGO–$ZnWO_4$–Fe_3O_4 nanocomposite as high performance visible light photocatalyst, RSC Adv. 6 (2016) 61821–61829.

[26] L. Lin, X. Zheng, S. Zhang, D.A. Allwood, Surface energy engineering in the solvothermal deoxidation of graphene oxide, Adv. Mater. Interfaces 1 (2014) 1300078.

[27] Y. Hernandez, V. Nicolosi, M. Lotya, F.M. Blighe, Z. Sun, S. De, I.T. McGovern, B. Holland, M. Byrne, Y.K. Gun'Ko, J.J. Boland, P. Niraj, G. Duesberg, S. Krishnamurthy, R. Goodhue, J. Hutchison, V. Scardaci, A.C. Ferrari, J.N. Coleman, High-yield production of graphene by liquid-phase exfoliation of graphite, Nat. Nanotechnol. 3 (2008) 563–568.

[28] K.A. Connors, J.L. Wright, Dependence of surface tension on composition of binary aqueous-organic solutions, Anal. Chem. 61 (1989) 194–198.

[29] D. Khossravi, K.A. Connors, Solvent effects on chemical processes. 3. Surface tension of binary aqueous organic solvents, J. Solut. Chem. 22 (1993) 321–330.

[30] H.P. Mungse, O.P. Sharma, H. Sugimura, O.P. Khatri, Hydrothermal deoxygenation of graphene oxide in sub-and supercritical water, RSC Adv. 4 (2014) 22589–22595.

[31] K. Hu, X. Xie, T. Szkopek, M. Cerruti, Understanding hydrothermally reduced graphene oxide hydrogels: from reaction products to hydrogel properties, Chem. Mater. 28 (2016) 1756–1768.

[32] L. Chen, X. Li, C. Ma, M. Wang, J. Zhou, Interaction and quantum capacitance of nitrogen/sulfur Co-doped graphene: a theoretical calculation, J. Phys. Chem. C 121 (2017) 18344–18350.

[33] M.M. Khoshdel, E. Targholi, M.J. Momeni, A first principle calculation of quantum capacitance of Co-doped graphenes as supercapacitor electrodes, J. Phys. Chem. C 119 (2015) 26290–26295.

[34] C. Song, J. Wang, Z. Meng, F. Hu, X. Jian, Density functional theory calculation for quantum capacitance of graphene oxide as supercapacitor electrodes, ChemPhysChem 19 (2018) 1579–1583.

[35] F. Barzegar, A.A. Khaleed, F.U. Ugbo, K.O. Oyeniran, D.Y. Momodu, A. Bello, J.K. Dangbegnon, N. Manyala, Cycling and floating performance of symmetric supercapacitor derived from coconut shell biomass, AIP Adv. 6 (2016) 115306.

[36] K.O. Oyedotun, M.J. Madito, A. Bello, D.Y. Momodu, A.A. Mirghni, N. Manyala, Investigation of graphene oxide nanogel and carbon nanorods as electrode for electrochemical supercapacitor, Electrochim. Acta 245 (2017) 268–278.

[37] T. Deng, W. Zhang, O. Arcelus, D. Wang, X. Shi, X. Zhang, J. Carrasco, T. Rojo, W. Zheng, Vertically co-oriented two dimensional metal-organic frameworks for packaging enhanced supercapacitive performance, Commun. Chem. 1 (2018) 6.

[38] M.K. Sahoo, P. Gogoi, G. Rajeshkhanna, S.V. Chilukuri, G.R. Rao, Significance of optimal N-doping in mesoporous carbon framework to achieve high specific capacitance, Appl. Surf. Sci. 418 (2017) 40–48.